Environment International 178 (2023) 108083

Contents lists available at ScienceDirect

Environment International

journal homepage: www.elsevier.com/locate/envint

Full length article

Spatio-temporal structures of satellite-derived water quality indicators along the Korean South Coast

Hae-Cheol Kim [a], Seunghyun Son [b,c], Chun Ok Jo [d], Yong Hoon Kim [e], Mingyu Park [f], Young-Gyu Park [g], Jongseong Ryu [h,*]

[a] SAIC at NOAA/NWS/NCEP/EMC, College Park, MD, USA
[b] NOAA/NESDIS Center for Satellite Applications and Research, College Park, MD, USA
[c] Cooperative Institute for Satellite Earth System Studies, Earth System Science Interdisciplinary Center, University of Maryland, College Park, MD, USA
[d] OceanScitech, Inc., Seoul, Republic of Korea
[e] Department of Earth and Space Sciences, West Chester University of Pennsylvania, West Chester, PA, USA
[f] Department of Atmospheric and Oceanic Sciences, Princeton University, Princeton, NJ, USA
[g] Ocean Circulation and Climate Research Department, Korea Institute of Ocean Science and Technology, Busan, Republic of Korea
[h] Department of Biotechnology, Anyang University, Ganghwa-gun, Incheon, Republic of Korea

ARTICLE INFO

Handling Editor: Adrian Covaci

Keywords:
VIIRS
Sea Surface Temperature
Chlorophyll *a*
Total Suspended Solids
Principal Component Analysis
Cross Spectral Analysis

ABSTRACT

The structure of 9-year time series data for Sea Surface Temperature (SST), Chlorophyll *a* (Chl-a) and Total Suspended Solids (TSS), derived from the Visible Infrared Imaging Radiometer Suite (VIIRS), was examined in this study. Authors found that there exists strong seasonality among the three variables with spatial heterogeneity along the Korean South Coast (KSC). In specific, SST was in phase with Chl-a, but out of phase with TSS by six months. A strong inversed spectral power with six-month phase-lag was found between Chl-a and TSS. This could be attributed to different dynamics and environmental settings. For example, Chl-a concentration seemed to have strong positive correlation with SST indicating typical seasonality of marine biogeochemical processes such as primary production; while a strong negative correlation between TSS and SST might have been influenced by changes in physical oceanographic processes, such as stratification and monsoonal wind-driven vertical mixing. In addition, the strong east–west heterogeneity of Chl-a suggests that the marine coastal environments are predominantly governed by distinct local hydrological conditions and human activities associated with land cover and land use, while the east–west spatial pattern revealed in TSS timeseries was associated with the gradient of tidal forcings and topographical changes keeping tidally induced resuspension low eastward.

1. Introduction

Coastal and estuarine waters are important habitats of ecologically and commercially important marine resources and provide socio-economic benefits and values. However, due to increased human activities and global climate change, coastal and estuarine systems have been facing unprecedented environmental challenges such as deterioration of water quality (WQ) (Anderson et al., 2002; Diaz and Rosenberg, 2008; Doney, 2010; Howarth et al., 2011; Rabalais et al., 2002; Rosenzweig et al., 2007). As freshwater inflow is the major source of nutrients and sediments delivered downstream, altered quantity and quality of riverine inputs and its contents are one of environmental concerns that can enhance harmful algal blooms, hypoxia downstream. Water quality in bays, estuaries and coastal waters also depends on their topographical/morphological settings (e.g., depth, size, shape) and/or local hydrodynamic conditions (e.g., currents, tidal forcings) from their downstream boundaries. Therefore, gaining knowledges on the spatio-temporal changes of WQ dynamics at the land–ocean boundaries and their implications require holistic approaches across the disciplines, such as environmental/marine sciences and socio-economics.

Although there still exist uncertainties in calibrating signals obtained from CASE II waters and in extracting meaningful WQ information, remote sensing can provide comprehensive datasets covering much larger areal coverage in relatively higher spatio-temporal resolution as compared to conventional field monitoring approaches. Recently, much attention has been paid to this gap-filling capability and the application

* Corresponding author.
E-mail address: jsryu@anyang.ac.kr (J. Ryu).

https://doi.org/10.1016/j.envint.2023.108083
Received 28 February 2023; Received in revised form 23 May 2023; Accepted 2 July 2023
Available online 3 July 2023

of remote sensing techniques becomes more common in monitoring WQ indicators (e.g., chlorophyll *a* [Chl-a]) in coastal and estuarine waters (Blondeau-Patissier et al., 2014; Bresciani et al., 2014; Kim et al., 2017, 2020; Lu et al., 2020; Mouw et al., 2015). Along with temperature, major organic/inorganic nutrient species, dissolved oxygen, heavy metals, Chl-a and total suspended solids (TSS) are representative standard WQ indicators commonly found in any conventional in-situ monitoring programs. Recently, Chl-a and TSS are getting more attentions as good examples in coastal satellite oceanography as well as oceanic remote sensing studies.

There have been extensive oceanographic studies around bays, estuaries and adjacent waters of the Korean South Coast (KSC). Some of them focused on physico-chemical features of the coastal waters (Kim, 1999; Kim and Rho, 1993, 1994; Kwon and Kang, 2007; Lee et al., 2018a; Yang, 1994; Yang et al., 1998) and some studies focused their efforts more on water quality issues of bays and estuaries, such as eutrophication and hypoxia (Cho, 1991; Hong et al., 1991; Kim et al., 2006, 2015b, Lee et al., 2017, 2018b; Lim et al., 2006). Yet, little or no efforts have been made to address spatio-temporal structures of interactive dynamics between satellite-derived Chl-a and TSS, and their relationships with SST (sea surface temperature) in larger regional scale that covers entire KSC (about 300–400 km in length). The research objectives of this paper include: 1) decomposing spatial and temporal variability of SST, Chl-a and TSS; 2) finding their relationships in the KSC waters; and 3) examining potential climatic implications embedded in the long-term timeseries of Chl-a.

2. Materials and methods

2.1. Study area

The Korean South Coast is a typical ria coast where there are several parallel rias separated by prominent ridges, forming a few major bays with large tidal flats extending a distance inland and numerous islands (Fig. 1; Park and Yi, 1995). The morphology of the KSC is a result of sea level change that caused the submergence of a river valley through geological processes of uplifts and subsidences during the late Holocene era (Kong and Park, 2007; Yoo et al., 2020).

Tides are predominantly semi-diurnal in the study area. Macrotidal setting is another characteristic feature in the KSC. The maximum tidal range is relatively large in the western KSC (e.g., ~300 cm) and getting decreased toward the eastern KSC (e.g., ~100 cm). The KSC, as part of the Korea/Tsushima Strait, is under the strong influence of Tsushima Warm Currents with the general northeastward flow from the East China Sea toward East/Japan Sea (Teague et al., 2002; Lee et al., 2019). The hydrographic data analysis results show an increase in the averaged salinity from the western Korea Strait toward eastern section due mainly to freshwater inputs from the Yangtze River (Hwang et al., 2014; Lee et al., 2019). In addition, cold and less saline water represents the tidally mixed coastal waters around KSC, which is separated from warm and saltier water mass influenced by the main branch of Tsushima Warm Current water mass (Lee et al., 2019).

In accordance with the Article 13 of Marine Conservation Act in Korea, the study area is divided into seven sections based primarily on the classification of coastal geography, the impact of river input, the characteristics of drainage basin, and the level of connectivity to the open ocean. Major freshwater input into the study area is from the Seomjin and Nakdong Rivers. The Seomjin River drains to the middle of the study area, i.e., into the section A4, while the Nakdong River enters to the eastern section, A6 (Fig. 1). The mean annual discharge of the Seomjin River ranges 58–68 m^3/s and it reaches up to 344 m^3/s in the Nakdong River (Hwang et al., 2017; Seo and Park, 2020). The catchment area of the Nakdong River is 23,300 km^2 which is about six times larger than that of the Seomjin River (4,832 km^2; Seo and Park, 2020).

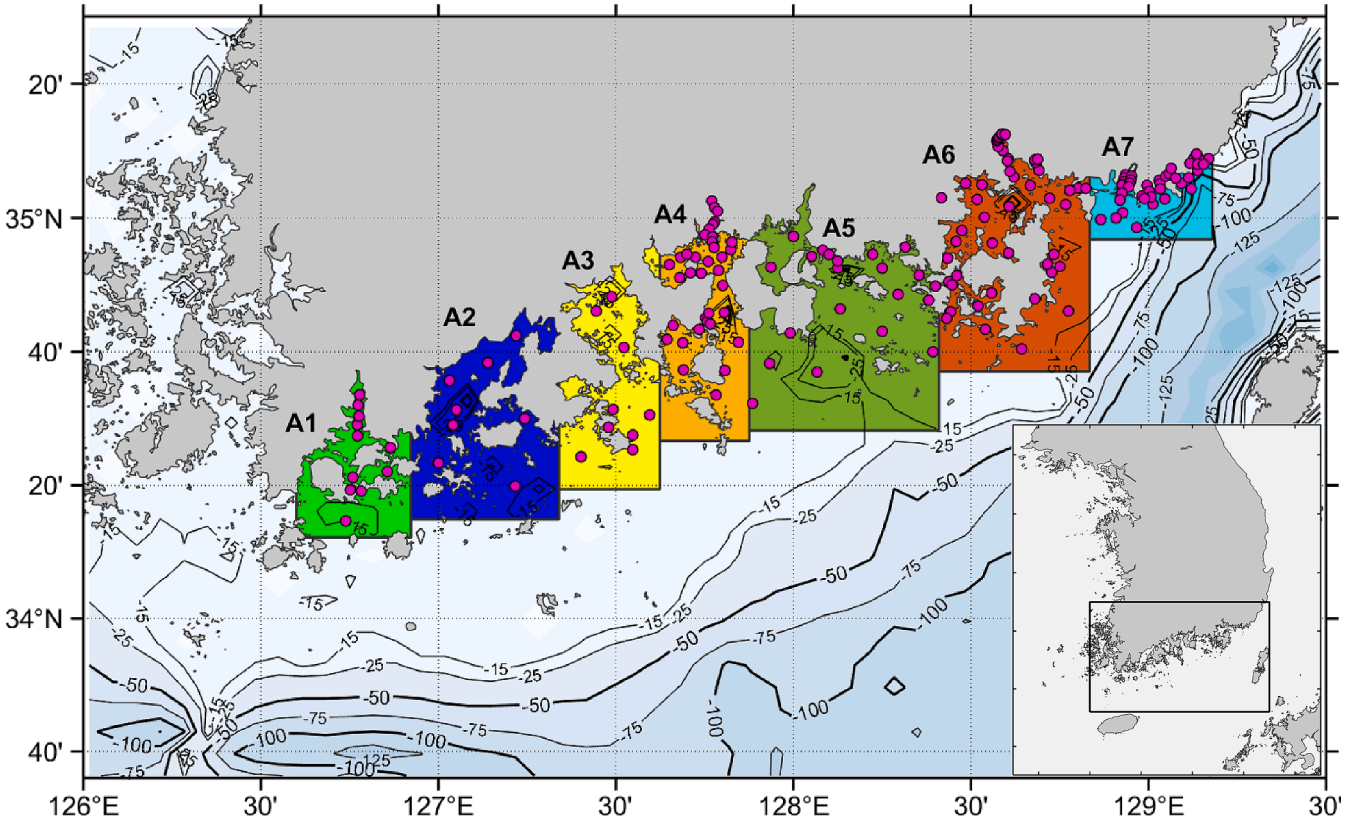

Fig. 1. Map of Korean South Coast and seven delineated boxes in the present study.

2.2. Satellite-derived observations

The Visible Infrared Imaging Radiometer Suite (VIIRS) is a multi-disciplinary instrument on the spacecraft, the Suomi National Polar-orbiting Partnership (S-NPP) which was successfully launched in October 2011. The mission is to provide continuity with the MODIS (Moderate Resolution Imaging Spectroradiometer) instrument and add to the moderate-resolution, long-term data record of WQ monitoring in estuaries as MODIS nears the end of its mission.

VIIRS-SNPP Level-2 daily ocean color products such as Chl-a and remote sensing reflectance (R_{rs}) at various wavelengths ($R_{rs}(\lambda)$), and day time SST from January 2012 to December 2020 were downloaded from the NASA ocean color website (http://oceancolor.gsfc.nasa.gov/) maintained by the Ocean Biology Processing Group (OBPG) of NASA Goddard Space Flight Center (GSFC) for the southern sea of Korean Peninsula (Fig. 1).

The VIIRS level-2 ocean color data were generated with the NASA standard atmospheric correction algorithm (Bailey et al., 2010; Stumpf et al., 2003). The VIIRS Chl-a data are derived using the NASA standard ocean color Chl-a algorithm (Hu et al., 2012; O'Reilly et al., 2000) and the VIIRS SST products are derived using the long-wave infrared (LWIR) SST algorithm with MODIS bands at 11 and 12 μm. The LWIR SST algorithm is based on a modified version of the nonlinear SST algorithm (Walton et al., 2004; Minnett et al., 2014; Kilpatrick et al., 2015). More information can be found at the NASA OBPG website (https://oceancolor.gsfc.nasa.gov/atbd/). Those Level-2 data were resampled to a standard Mercator projection with 1 km spatial resolution for the study area.

A TSS model developed for the Korean coastal waters was adopted for this study (Siswanto et al., 2011; Son et al., 2014).

$$\log(\mathrm{TSS}) = 0.649 + 25.623[R_{rs}(\lambda_2) + R_{rs}(\lambda_3)] - 0.646[R_{rs}(\lambda_1)/R_{rs}(\lambda_2)] \quad (1)$$

where $R_{rs}(\lambda)$ is remote sensing reflectance at various wavelengths $\lambda_1 = 490$ nm, $\lambda_2 = 555$ nm, $\lambda_3 = 670$ nm. In this paper, the TSS algorithm using $R_{rs}(\lambda)$ at 3 wavelengths ($\lambda_1 = 486$ nm, $\lambda_2 = 551$ nm, $\lambda_3 = 670$ nm) were applied to the daily VIIRS ocean color data to produce TSS maps in the study area. Various composite images of the VIIRS-SNPP Chl-a, SST, and TSS data were generated using the daily remapped VIIRS to investigate spatial and temporal distribution of Chl-a, SST, and TSS in the vicinities of KSC. The average values of the monthly VIIRS-derived Chl-a, SST, and TSS images extracted from the 7 regions (Fig. 1) were used to generate the monthly time series.

2.3. Statistical analyses

The principal component analysis (PCA) was used to decompose VIIRS time series data from the 7 regions and to examine spatio-temporal structure of SST, Chl-a and TSS. Principal component analysis is the same as empirical orthogonal function (EOF) often used when extracting spatial structures by decomposing multi-dimensional and multivariate data in physical oceanography. Authors applied the PCA to a group of 7 time series from the study area and created a new time series of scores which has the same length as the original time series, and the eigenvectors of covariance matrices (a.k.a., loadings) were also computed. The dimension of loadings is the same as that of the spatial locations in the data (7 regions in this study). The time series of PC1 (or EOF mode 1) in the coherent variation (scores) explained temporal pattern and was then filtered removing seasonality to see inter-annual variability. The filtered time series of PC1 from each variable (SST, Chl-a, TSS) was converted to power spectrum using cross-spectral analysis to compute lags between any chosen two time-series (e.g., SST vs. Chl-a; SST vs. TSS). The cross-spectral analysis is a statistical method to find signs that determine lags between any two time-series and how much the two time-series correlated either positively or negatively. Cross spectral power gives frequencies of the two time-series when converted from time domain to frequency domain, and cross-correlation coefficients are the indicator of the lag where the two time-series are best aligned.

Filtered time series of PC1 from SST and Chl-a was also compared against a climate index, West Pacific (WP). The WP pattern, a primary mode of low-frequency variability over the North Pacific, is one of the major teleconnection patterns over the wintertime Northern Hemisphere (Barnston and Livezey, 1987; Wallace and Gutzler, 1981). This dominant pattern of low-frequency variability in the winter season may cause changes in storm track (Nakamura et al., 1987; Lau 1988; Linkin and Nigam 2008; Tanaka et al., 2016) which can cause precipitation extremes over the Pacific and North America (Nigam 2003; Linkin and Nigam 2008; Yuan et al., 2015). The WP pattern is also associated with surface air temperatures over the lower latitudes of the western North America, East Asia, and the Far East (Linkin and Nigam, 2008; Takaya and Nakamura, 2005a,b; Tanaka et al., 2016) and modulates the East Asian Winter Monsoon (EAWM; Takaya and Nakamura 2013; Pak et al., 2014; Wang and Chen 2014). Monthly WP data were obtained from the Climate Prediction Center (CPC) of National Centers for Environmental Prediction (NCEP) at National Oceanic and Atmospheric Administration (NOAA) (www.cpc.ncep.noaa.gov/data/indices/).

3. Results and discussion

3.1. Long-term VIIRS-SNPP climatology (2012–2020)

Climatology images from January 2012 to December 2020 of VIIRS SST, Chl-a, and TSS were produced using the daily remapped VIIRS data for the KSC to investigate the average spatial distribution (Fig. 2). The long-term climatological pattern of SST exhibits high SST in offshore waters which, presumably, might have been influenced by variations in the bifurcation of the Kuroshio Current and origin of the Tsushima Warm Current (Lie and Cho, 2002; Ichikawa and Beardsley, 2002), while SST along the coasts is relatively lower than that of offshore waters (Fig. 2a). Nevertheless, the long-term SST mean values are found to have not much discrepancies among the 7 regions (Fig. 2d).

The Chl-a image shows clearly divided spatial distribution between offshore and nearshore waters with lower Chl-a in the offshore waters and much higher Chl-a along the coasts (Fig. 2b). Additionally, Chl-a concentrations are higher in the eastern coastal waters than those in the western coastal waters, which is confirmed by the long-term mean Chl-a (Fig. 2e). It is noteworthy that high Chl-a concentration in A6 is owing to the Jinhae Bay waters known as very highly eutrophic coastal waters (Kim et al., 2014a; Lee and Kim, 2008; Lim et al., 2006; Yoon et al., 2019). This is mainly due to anthropogenic activities since 1970′s (e.g., rapid industrialization/urbanization and intensive aquaculture) (Kim et al., 2012a,b; Kwon et al., 2014), which resulted in chronic seasonal hypoxia, water quality deterioration, and harmful algal blooms.

The overall pattern of the TSS image is similar to that of Chl-a, higher in the nearshore waters and lower in the offshore waters (Fig. 2c). However, as opposed to the spatial distribution of the Chl-a, TSS is much higher in the western coastal waters than in the eastern waters as seen in Fig. 2f. This feature is associated with local resuspensions due to tidal forcings and topographical change, i.e., wider continental shelf on the western KSC than on the eastern sections. Along the southern coast of Korea both tidal range and current decrease from the west to the east (Byun and Hart 2022). For example, the M2 tidal amplitude is about 100 cm on the western waters (A1 region in Fig. 1), while that on the eastern side (A7 region in Fig. 1) is about 40 cm. Therefore, tidal resuspension would decrease eastward. In addition, in A5 region, there is a channel extending southeastward normal to the coast. This sudden change in water depth would reduce resuspension drastically to form a boundary for high TSS as can be seen from Fig. 2c. This is more distinctive in the Jinhae Bay (A6) where TSS is relatively lower, but Chl-a concentration is significantly high. It is a semi-enclosed inner bay, and the exchange with open ocean is rather limited. Since the 1970 s, the inflow of sewage and

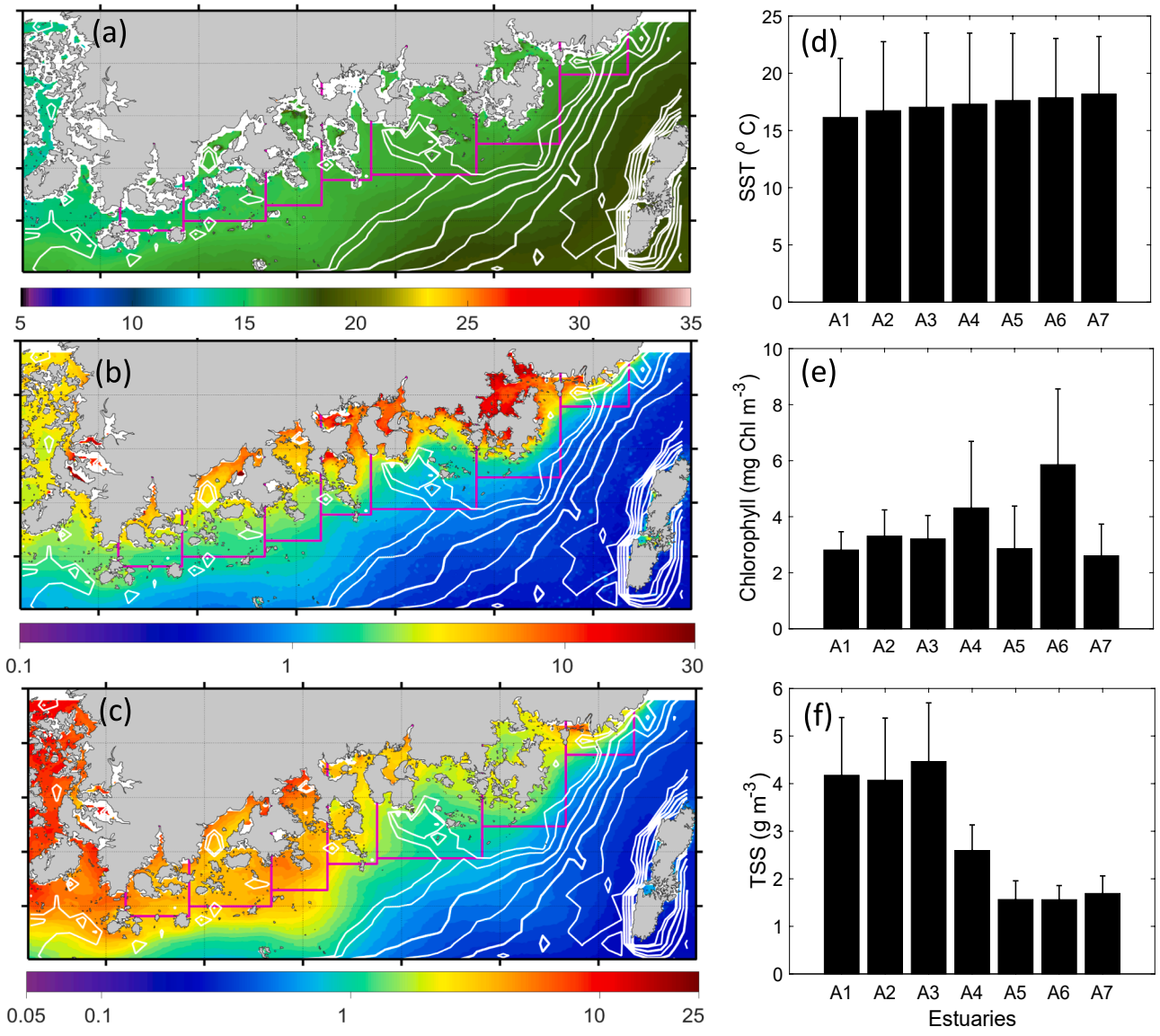

Fig. 2. Distributions of long-term climatology of (a) SST (°C), (b) Chl-a (mg/m^{-3}(−|-)) and (c) TSS (g/m^{-3}(−|-)) with mean and standard deviation (error bars) of (d) SST (°C), (e) Chl-a (mg m $^{-3}$) and (f) TSS (g/m^{-3}(−|-)) at each box.

wastewater has rapidly increased due to industrial development and urbanization, resulting in eutrophication and consequently high Chl-a concentration. Fig. 3 illustrates that synoptic distributions of the VIIRS-derived climatology for the Chl-a and TSS reveal similar patterns to those gridded observation composited from 2012 to 2020.

3.2. Monthly VIIRS-SNPP climatology and seasonal variations

Monthly climatological (2012–2020) images of VIIRS SNPP SST, Chl-a, and TSS for the KSC waters are presented in Fig. 4. The overall spatial distribution of the monthly climatological images is similar to that from the climatological images in SST, Chl-a, and TSS. However, there is a strong seasonal variation in SST, Chl-a, and TSS images. The monthly climatology VIIRS-derived SST images show that SST is lowest in winter (January and February) and higher in July to September with the highest in August (Fig. 4). Some bays (Deungnyang (A2), Yeoja (A3) and Jinhae Bay (A6)) surrounded by islands revealed relatively higher SST than nearshore waters during summer months (June through September), which is, presumably, due to their semi-enclosed morphological characteristics and shallow depths that reduce the exchange of water mass. As a result, the temperature variations of these inner areas are highly correlated with those in air temperature (Park et al., 2017).

In most of the nearshore coastal areas, Chl-a concentrations are relatively high during growing seasons (May through October with highest peak in September), whereas Chl-a in the offshore waters is higher in spring and autumn (spring and fall blooms) and lower in summer and winter, which is a typical seasonal variation of phytoplankton in temperate seas. The mid- to late summer Chl-a peak in the nearshore waters of KSC including bays and estuaries can be explained in several aspects: increased nutrients input carried by increased freshwater inflows during episodic storm events or by increased precipitations during summer Asian monsoon (Jang et al., 2005; Jang et al., 2010); increased phosphate (PO_4^{3-}) discharges from industrialized and urbanized point sources (Kim et al., 2015a; Lee et al., 2001; Lim et al., 2012); increased ammonium (NH_4^+) input from sediment through denitrification (Kemp and Boynton, 1992; Kim et al., 2012a,b; Ryther et al., 1972); increased phosphate (PO_4^{3-}) from hypoxic sediment via desorption of iron-bound phosphorus (Jensen et al., 1995; Jordan et al., 1991; Conley et al., 2002; Howarth et al., 2011) and extensive aquaculture systems (Lee and Kim, 2008).

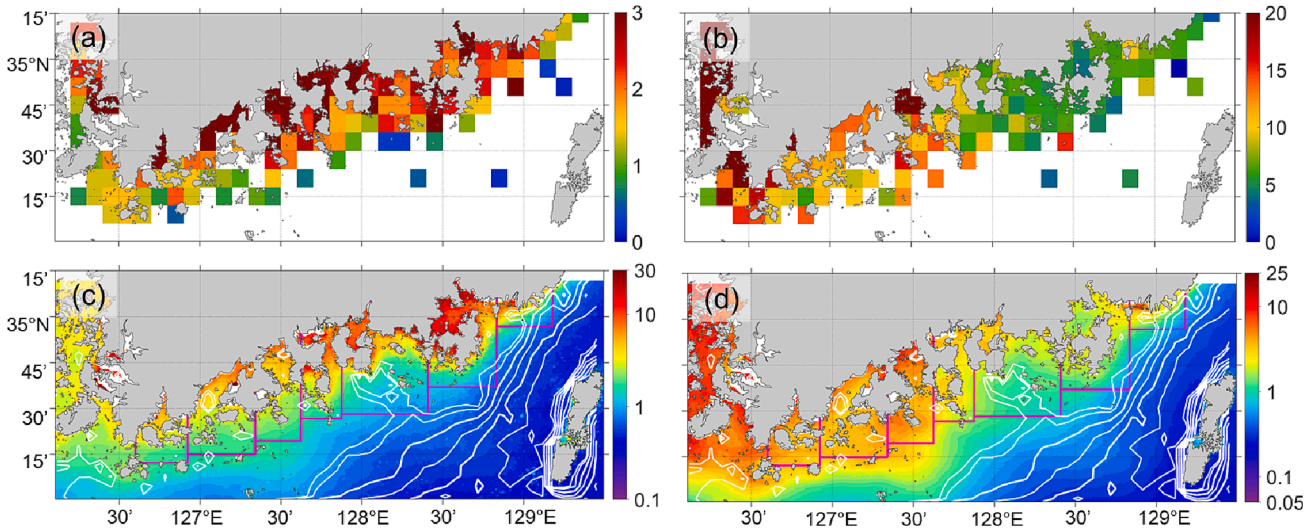

Fig. 3. Comparisons of mean in-situ climatology (2012–2020) of (a) Chl-a (mg/m^{-3}(−|-)), (b) TSS (g/m^{-3}(−|-)) against VIIRS-derived (c) Chl-a (mg/m^{-3}(−|-)), (d) TSS (g/m^{-3}(−|-)).

The monthly TSS climatology reveals that higher TSS levels gradually decreases from coast to offshore, which is similar to the nearshore-to-offshore gradient shown in Chl-a. However, as opposed to Chl-a, it is found that elevated TSS concentration occurs during the winter months (December through March) while TSS levels in summer (July through September) remain low (Fig. 4c). This seasonality of TSS is due, in large, to changes in the intensity of vertical mixing, which induces the resuspension of sediments. The high TSS concentration during winter months can be explained by intensified vertical mixing due to stronger monsoonal northwesterly wind (Lee et al., 2004; Hwang et al., 2014; Kim et al., 2014b; Son et al. 2014). During summer, not only the wind is weaker but also the combination of freshwater and strong solar heating enhances surface stratification (Park et al., 2021), which reduces the vertical mixing and subsequently TSS resuspension. For instance, Bae and Kim (2011) calculated the stratification factor based on the total flow of tide, wind and density effect and found that the distribution and magnitude of the stratification factor were different between the two seasons. In addition, it is also noteworthy that the east–west contrast in TSS concentrations is striking. The western regions have much higher and broader distributions of murky waters than those of eastern regions. The seasonal variations are more conspicuous in the western coastal waters (A1-A3) than in the eastern coastal waters (A5-A7). The spatial and temporal pattern of the two regions were also well described by the distribution of stratification (Bae and Kim, 2011).

3.3. Principal component analysis

Hovmöller diagrams that represent the temporal evolution of each variable clearly reveal the temporal profile of alternating patterns between positive (yellow) and negative (blue) anomalies (Fig. 5). For SST seasonal variability is found to be strong in all 7 regions along the KSC as presented in Fig. 5a. Although there is a weak interannual variability with 4- to 5-year interval (e.g., see color concentrations of yellow bands in Fig. 5a), SST time series is characterized by the intra-annual variability (i.e. season), presumably, driven by warming-cooling processes of the area. For Chl-a seasonality is not as clear as that of SST (Fig. 5b). The Hovmöller diagram shows stronger inter-annual variability as compared to SST, and for a certain year band not all those 7 regions are found to have homogeneous distribution unlike that shown in SST, which is the similar case for TSS (Fig. 5c). Temporal evolution of TSS anomaly pattern is not homogeneous along the 7 regions of the KSC. Some regions have higher concentrations in one season than the other regions and vice versa. The patterns of Chl-a and TSS indicate that more complex processes might have been involved in their dynamics than those governing SST dynamics.

To decompose the spatio-temporal structure of the time series datasets, a principal component analysis (a.k.a., empirical orthogonal function; EOF) was applied to the long-term time series of VIIRS-derived monthly SST, Chl-a and TSS from 7 regions (Fig. 6). Each data set has 9-year long records in monthly intervals from 7 regions (thus, 108 × 7 dimension) and computed eigenvector and eigen values of covariance can explain variability of each time series. After all principal components are decomposed into orthogonal positions, variation of each time series is illustrated on a biplots (Fig. 6a-c). Each X- (PC1) and Y-axis (PC2) represents temporal and spatial structure of the datasets. The loadings (eigenvector of the covariance matrix) from the each VIIRS-derived SST, Chl-a and TSS for the 7 regions are represented with lines, respectively (Fig. 6a-c). Notice that loadings from SST, Chl-a and TSS times series are located on the positive axis of PC1, representing their temporal structure. This explains that all 7 regions have strong seasonal patterns. For instances, the percent of explained SST variances in PC1 and PC2 is 99.1% and 0.6%, respectively (Fig. 6d). The percent of explained Chl-a variance is 60.4% in PC1 and 15.7% in PC2 (Fig. 6e). Similarly, 64.0% of TSS variance can be explained by PC 1 and 19.5% by PC2 (Fig. 6f). As seen in Fig. 6, the time component (seasonality) predominantly explains the structure of SST time series. Although the PC1 (seasonality) is also a major player determining the structure of Chl-a and TSS, spatial component (PC2) is not negligible in contributions to the variance of these two variables. Interestingly, loadings from each region are clustered into two groups along the PC2 axis for both Chl-a and TSS (see red and blue circles in Fig. 5b and 5c). Bays, estuaries and coastal waters in the western part of the KSC (A1-A3) are grouped in the positive axis of the PC2 for Chl-a and negative axis of the PC2 for TSS time series (red circles in Fig. 5b and 5c). On the contrary, the regions located on the eastern part of the KSC (A4-A7) are grouped in the negative axis of the PC2 for Chl-a and positive axis of the PC2 for TSS time series (blue circles in Fig. 5b and 5c). This indicates that both Chl-a and TSS have east–west spatial heterogeneity at any given time points and the pattern is inversed between the two variables.

3.4. Cross spectral analysis

Cross spectral analysis was performed to examine the spectral power of individual time series, their correlation, and phase lags (Figs. 7-9). It was found that the time series of PC1 in the coherent variation (scores) for VIIRS-derived monthly SST and Chl-a were in-phase (Fig. 7a) with

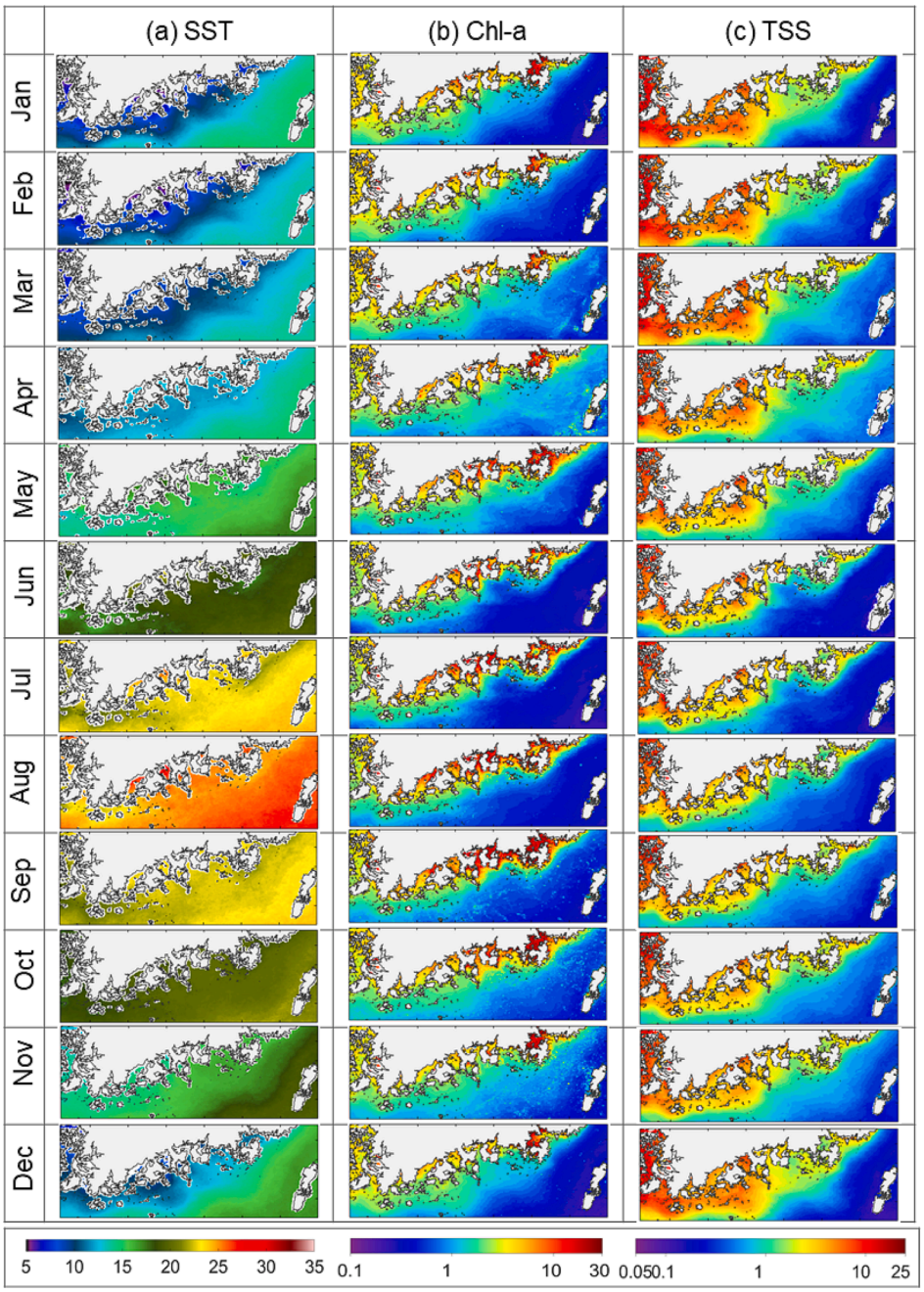

Fig. 4. Distributions of monthly climatology of (a) SST (°C), (b) Chl-a ($mg/m^{-3}(-|-)$) and (c) TSS ($g/m^{-3}(-|-)$).

strong power at the frequency of one year (Fig. 7b) with significant ($p < 0.05$) coherence within 95% confidence interval (Fig. 7c), which suggests the two time series have strong in-phase seasonal variability (positive correlation). The correlation coefficient of the two PC1 time series is 57% (Fig. 7d). For VIIRS derived monthly SST and TSS, the two variables' time series of PC1 in the coherent variation (scores) were out-of-phase (Fig. 8a) with a strong negative power spectrum at the frequency of one-year (Fig. 8b) with significant ($p < 0.05$) coherence within 95% confidence interval (Fig. 8c). This also suggests the two time series showed substantial out-of-phase seasonal variability (negative correlation). A 6-month phase-lag between the two PC1 time series was found and the correlation coefficient of the shift was 75% (Fig. 8d). The two time series of PC1 between the Chl-a and TSS were naturally found strong negative (out-of-phase) relationship (Fig. 9). The strong negative spectral power was at the frequency of one-year. This negative correlation was already presented in PCA structure (Fig. 5). One can note that these two groups (east vs. west regions) had an inverse relationship between the Chl-a and TSS time series. For example, those regions with positive PC2 (upper right quadrant) of Chl-a were located in the negative side of PC2 (lower right quadrant) in TSS, and on the contrary, those regions with negative PC2 (lower right quadrant) of Chl-a were located in the positive side of PC2 (upper right quadrant) in TSS (Fig. 6).

3.5. East-west spatial heterogeneity

The east–west spatial heterogeneity (Fig. 5b and 5c) between Chl-a and TSS in this study was somewhat similar to the north–south spatial heterogeneity found between the two variables in the Korean West Coast (KWC) previously reported (Kim et al., 2017). In their paper, they

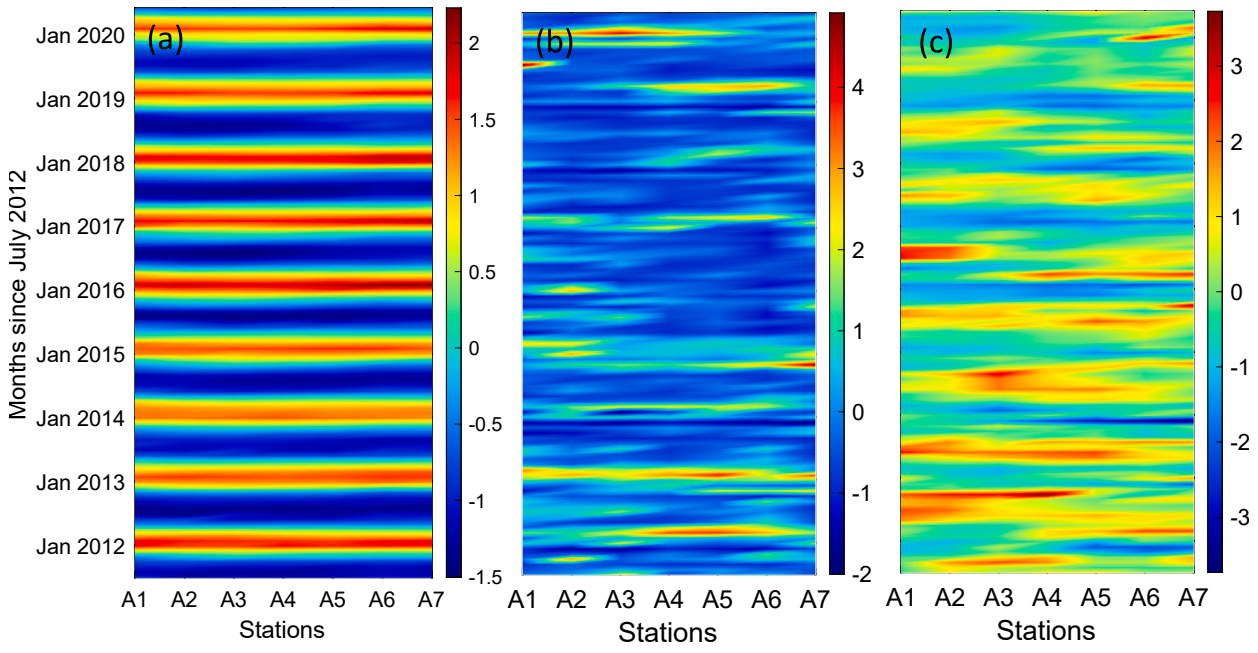

Fig. 5. A Hovmöller diagram showing temporal evolution of 10-year anomalies of (a) SST (°C), (b) Chl-a (mg/m^{-3}(−|-)) and (c) TSS (g/m^{-3}(−|-)) in seven boxes along the Korean South Coast.

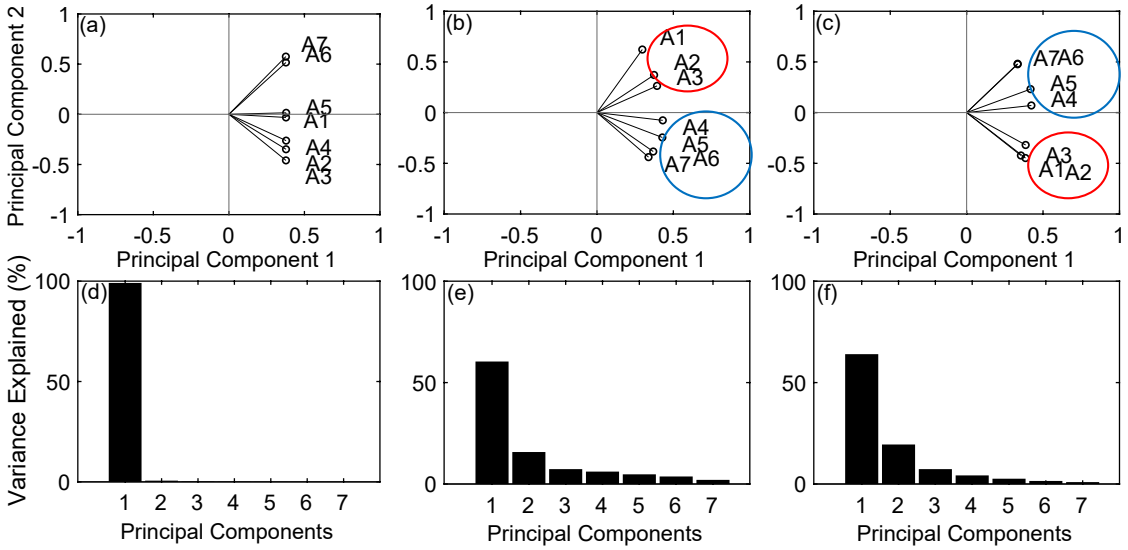

Fig. 6. Principal component analysis (PCA) of (a) SST (°C), (b) Chl-a (mg/m^{-3}(−|-)) and (c) TSS (g/m^{-3}(−|-)) for boxes along the Korean South Coast, which demonstrates spatial structures of timeseries of each variable. Bottom panels (d, e, f) present percentage that explains variance for all principal components. It is noteworthy that the box A1, A2, A3 (red circle) are located on the opposite quadrant of A4, A5, A6 and A7 (blue circle) along the principal component 2 axis indicating the spatial heterogeneity of the two environmental variables (Chl-a and TSS). (For interpretation of the references to color in this figure legend, the reader is referred to the web version of this article.)

summarized that both Chl-a and TSS concentrations were, in general, high along the KWC with north–south spatial patterns that can distinguish Chl-a departure from TSS images in the KWC (see Fig. 3 in Kim et al., 2017). During summer months, Chl-a concentration was found to be significantly high in some regions where TSS concentration remained relatively low and the opposite for the winter months (low Chl-a and high TSS). In the present study, the east–west spatial pattern in the KSC was clearly observed by visual inspection (Fig. 4), which is statistically confirmed by the principal component analyses with 16–20% of explanation power of the variances by PC2 (spatial component) (Fig. 6e,f). These results were comparable to those in KWC (see Fig. 6a and 6b in Kim et al., 2017). Despite the algorithmic limitation of CASE I ocean color product when applied to CASE II waters, the spatial distribution of VIIRS-derived Chl-a in the KSC still gave synoptic information about regional trends and patterns over larger areas and longer time periods, without necessarily having too much bias due to coastal TSS.

Then what caused the inversed heterogeneity in both Chl-a and TSS timeseries? The spatial variations in TSS can be explained as follows: 1) The bifurcation of the Kuroshio Current and complex nature of interacting dynamics of shelf water and Tsushima Warm Current, branched from the Kuroshio Current, governed the amount of allochthonous sediment delivery to the western regions of the KSC (Fig. 1 in Bi et al., 2018); 2) Tidal currents-induced resuspension was one of the most dominating processes in TSS dynamics of the western regions of the KSC

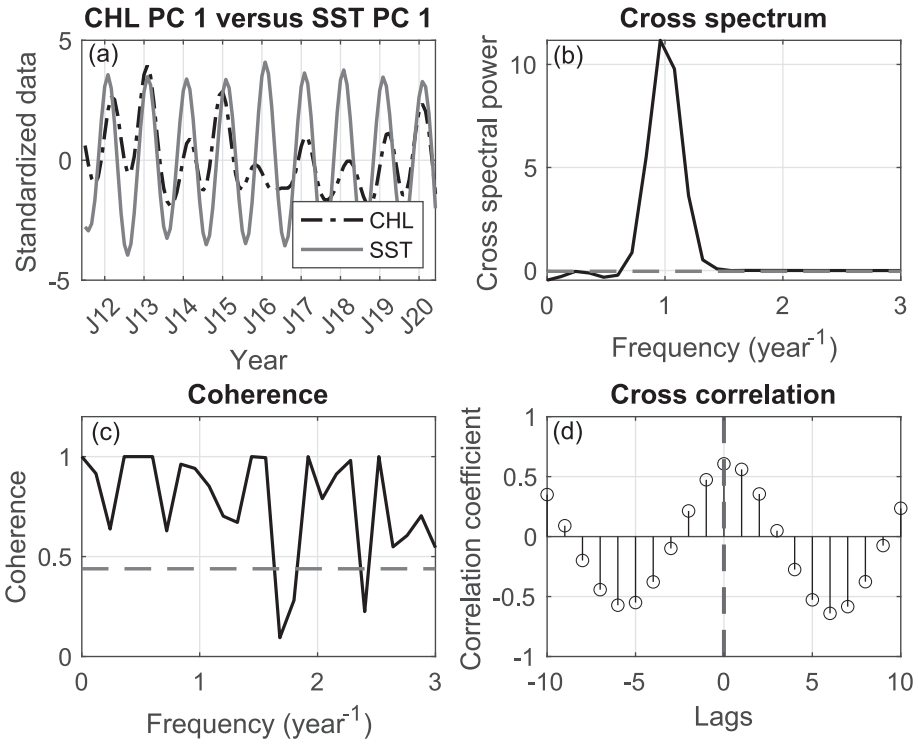

Fig. 7. (a) Butterworth filtered PC 1 (EOF mode 1) for Chl-a (mg/m^{-3}(−|-)) and SST (^{o}C), (b) cross spectral power between PC 1 for Chl-a (mg/m^{-3}(−|-)) and SST (^{o}C) at given spectral frequency bands, (c) coherence showing correlation coefficients for Chl-a (mg/m^{-3}(−|-)) and SST (^{o}C) at spectral frequency bands, (d) cross-correlation function with respect to lags explaining phase-shifts. Horizontal grey dashed lines represent upper limits of 95% confidence interval. Vertical grey dashed line represents phase-shift zero.

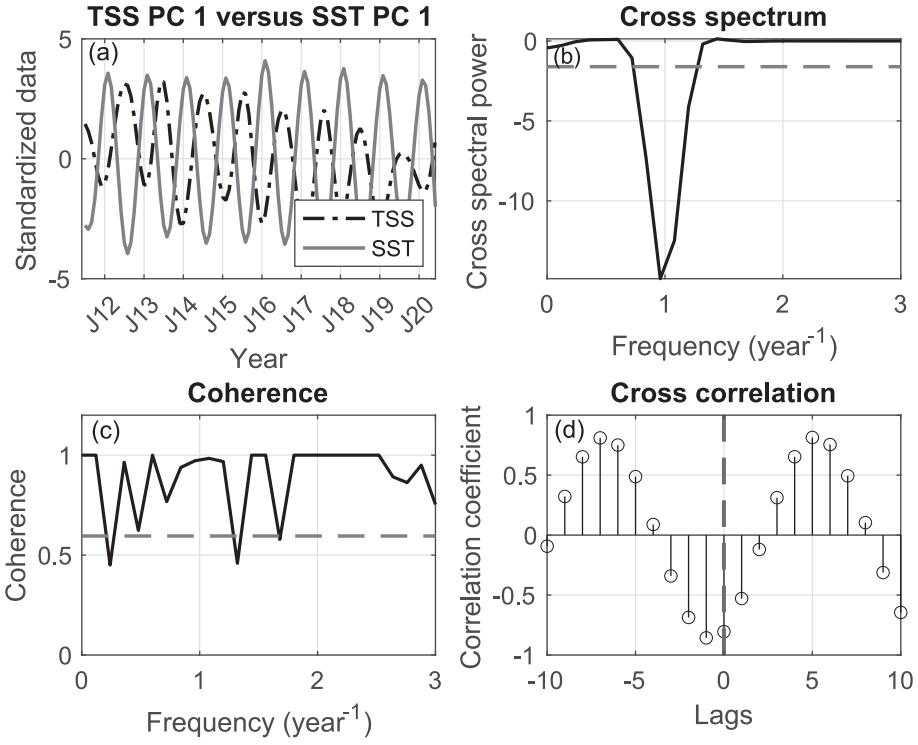

Fig. 8. (a) Butterworth filtered PC 1 (EOF mode 1) for TSS (g/m^{-3}(−|-)) and SST (^{o}C), (b) cross spectral power between PC 1 for TSS (g/m^{-3}(−|-)) and SST (^{o}C) at given spectral frequency bands, (c) coherence showing correlation coefficients for TSS (g/m^{-3}(−|-)) and SST (^{o}C) at spectral frequency bands, (d) cross-correlation function with respect to lags explaining phase-shifts. Horizontal grey dashed lines represent upper limits of 95% confidence interval. Vertical grey dashed line represents phase-shift zero.

(Lee et al., 2013; Son et al., 2014). Kim et al. (2017) reported that diurnal (hour-to-hour) variations in TSS assessed with Geostationary Ocean Color Imager (GOCI) clearly demonstrated that TSS dynamics in Wando Coast (near A1 in this study) was strongly influenced by tidal currents, such as tidal asymmetry effect in stratification as discussed in Son et al. (2014); 3) The seasonal variations in TSS was, presumably, connected with changes in the dominant wind (thus, surface current) patterns. The seasonal circulations in the eastern Yellow Sea were clockwise in winter and an anti-clockwise circulation in summer (Son et al., 2014), respectively. The southward coastal current may bring sediment originating from KWC toward western regions of KSC during winter months (Bi et al., 2018; Bian et al., 2013). In addition, the seasonality of TSS due to changes in intensity of stratification was more pronounced in the western region than eastern KSC (Bae and Kim, 2011); and 4) Coastal bathymetry between east and west (see the major bottom topographical change in A5 region in Fig. 1). Nearshore waters

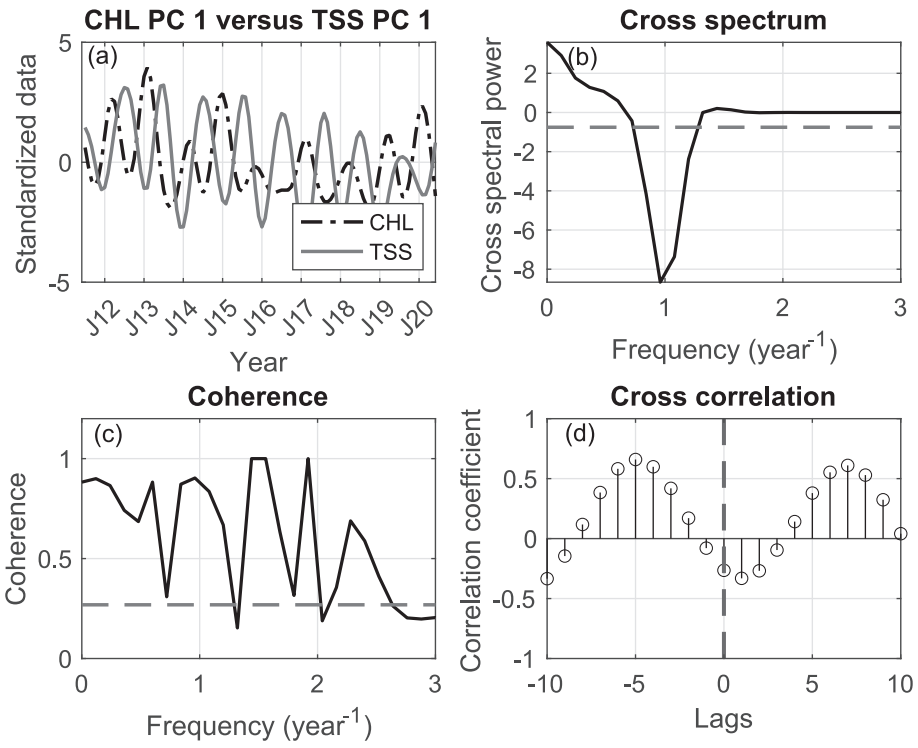

Fig. 9. (a) Butterworth filtered PC 1 (EOF mode 1) for Chl-a (mg/m^{-3}(−|-)) and TSS (g/m^{-3}(−|-)), (b) cross spectral power between PC 1 for Chl-a (mg/m^{-3}(−|-)) and TSS (g/m^{-3}(−|-)) at given spectral frequency bands, (c) coherence showing correlation coefficients for Chl-a (mg/m^{-3}(−|-)) and TSS (g/m^{-3}(−|-)) at spectral frequency bands, (d) cross-correlation function with respect to lags explaining phase-shifts. Horizontal grey dashed lines represent upper limits of 95% confidence interval. Vertical grey dashed line represents phase-shift zero.

along the KSC revealed spring phytoplankton blooms in some coastal regions or summer blooms in others. The timing and magnitude of the bloom climax occurred differently among the regions depending on the local environmental settings leading to east–west heterogeneity of Chl-a along the KSC. Possible explanations for this are as follows: 1) hydrological conditions, such as watershed size, freshwater inflow quantity, man-made damming, local climate conditions and morphological characteristics; 2) the land-cover land-use between the eastern and western regions is significantly different; 3) aqua culture systems in the vicinities of the coastal regions; and 4) atmospheric/oceanographic conditions, such as wind- and tidal forcings, circulation patterns, bottom bathymetry.

3.6. Climate implications

To investigate a potential linkage between the water quality indicators over the KSC and the WP pattern, cross spectral analysis was performed (Figs. S1 and S2). The results between the PC 1 time series for SST and the WP index suggest that they are negatively correlated (Fig. S1d) with the strongest signal at the frequency of one year (Fig. S1b) which exceeds 95% confidence level (Fig. S1c). This result indicates that, along the KSC, the positive phase of WP pattern is associated with cold SST during winter months, and vice versa for summer months. This result is physically consistent with the previous finding that the cold advection develops over the Korean Peninsula in the positive phase of the WP pattern (e.g., Fig. 3 in Tanaka et al., 2016). Regarding the cross spectral analysis result using the Chl-a PC1 time series (Fig. S2), its relationship with the WP teleconnection turns out to be negligible due to the small correlation value (Fig. S2d). This muted relationship might be partly caused by the east–west spatial heterogeneity of Chl-a over the KSC, which is correlated with the large-scale atmospheric circulation. However, it rather suggests that the role of atmospheric teleconnection in driving the water quality indicators such as Chl-a concentrations is quite limited with the given approach as it cannot capture subseasonal timescale of atmospheric circulations (e.g., Butterworth filter); the WP-driven patterns are, in general, found in the Western-Central North Pacific, where the KSC is located on the western boundary of the area; the present study focused on the seasonal cycle of phytoplankton dynamics not on seasonal characteristics. Although finding causalities between local phenomena and large-scale atmospheric patterns is a challenging task, it still deserves attention as more and more studies report climate-driven downscaled effect in the coastal marine ecosystems.

4. Conclusion

The structure of satellite retrievals of SST and two water quality indicators (Chl-a, TSS) in the KSC exhibits strong seasonality among the three variables. The PCA results indicate that there exists strong east–west heterogeneity in Chl-a and TSS with a clear six-month phase-lag of both water quality indicators against SST, implying their inversed seasonal variability. The strong east–west heterogeneity of Chl-a is influenced by local hydrological conditions and human activities. For example, the major estuaries and rivers are located on the eastern regions more than the west and this is also true for the urbanized and industrialized areas. The east–west heterogeneity of TSS is associated with the gradient of tidal forcings and topographical changes along the KSC that keep tidally induced resuspension low eastward. The negative correlation between Chl-a and TSS found in their cross spectral analysis is aliased relationships of Chl-a and TSS against SST, which indicates that seasonality of Chl-a in the KSC is determined by typical bottom-up biogeochemical processes, and that seasonality of TSS is more driven by changes in physical oceanographic processes. For example, during warm season more favorable light condition and increased freshwater inflow with anthropogenic nutrient loadings likely cause higher Chl-a concentration, while weak stratification and stronger vertical mixing during winter months increase more chances of TSS resuspension.

CRediT authorship contribution statement

Hae-Cheol Kim: Conceptualization, Methodology, Formal analysis, Visualization, Writing – original draft, Writing – review & editing. **Seunghyun Son:** Conceptualization, Data curation, Formal analysis, Writing – original draft. **Chun Ok Jo:** Visualization. **Yong Hoon Kim:**

Conceptualization, Writing – original draft, Writing – review & editing. **Mingyu Park:** Writing – original draft. **Young-Gyu Park:** Writing – review & editing. **Jongseong Ryu:** Conceptualization, Supervision, Funding acquisition.

Declaration of Competing Interest

The authors declare that they have no known competing financial interests or personal relationships that could have appeared to influence the work reported in this paper.

Data availability

Data will be made available on request.

Acknowledgments

The research was supported by Korea Institute of Marine Science & Technology Promotion (KIMST), funded by the Ministry of Oceans and Fisheries (MOF), Korea, titled "Integrated Management of Marine Environment and Ecosystems Around Saemangeum (20140257)'', "Development of Advanced Science and Technology for Marine Environmental Impact Assessment (20210427)'', "Development of Living Shoreline Technology Based on Blue Carbon Science toward Climate Change Adaptation (20220526)'', "Monitoring Environmental and Ecological Changes in Dynamic Coasts and Estuaries of the Korean four Major Rivers (RS-2023-00238486)" and "Development of Risk Managing Technology Tackling Ocean and Fisheries Crisis around Korean Peninsula by Kuroshio Current (RS-2023-00256330)". These scientific results and conclusions, as well as any views or opinions expressed herein, are those of the author(s) and do not necessarily reflect those of NOAA or the US Department of Commerce.

Appendix A. Supplementary data

Supplementary data to this article can be found online at https://doi.org/10.1016/j.envint.2023.108083.

References

Anderson, D.M., Glibert, P.M., Burkholder, J.M., 2002. Harmful algal blooms and eutrophication: nutrient sources, composition, and consequences. Estuaries 25, 704–726. https://doi.org/10.1007/BF02804901.

Bae, S.W., Kim, D.S., 2011. Seasonal variation of coastal front by numerical simulation in the southern sea of Korea. J. Environ. Sci. Int. 20 (9), 1141–1149. https://doi.org/10.5322/JES.2011.20.9.1141 in Korean.

Bailey, S., Franz, B., Werdell, J., 2010. Estimation of near-infrared water leaving reflectance for satellite ocean color data processing. Optics Express 18, 7521–7527. https://doi.org/10.1364/OE.18.007521.

Barnston, A.G., Livezey, R.E., 1987. Classification, seasonality, and persistence of low-frequency atmospheric circulation patterns. Mon. Weather Rev. 115, 1083–1126. https://doi.org/10.1175/1520-0493(1987)115<1083:CSAPOL>2.0.CO;2.

Bi, R., Chen, X., Zhang, J., Ishizaka, J., Zhuang, Y., Jin, H., Jin, H., Zhang, H., Zhao, M., 2018. Water mass control on phytoplankton spatiotemporal variations in the northeastern East China Sea and the western Tsushima Strait revealed by lipid biomarkers. J. Geophys. Res.: Biogeosci. 123, 1318–1332. https://doi.org/10.1002/2017JG004340.

Bian, C., Jian, W., Greatbatch, R.J., 2013. An exploratory model study of sediment transport sources and deposits in the Bohai Sea, Yellow Sea, and East China Sea. J. Geophys. Res.: Ocean 118, 5908–5923. https://doi.org/10.1002/2013JC009116.

Blondeau-Patissier, D., Gower, J.F.R., Dekker, A.G., Phinn, S.R., Brando, V.E., 2014. A review of ocean color remote sensing methods and statistical techniques for the detection, mapping and analysis of phytoplankton blooms in coastal and open oceans. Prog. Oceanogr. 123, 123–144. https://doi.org/10.1016/j.pocean.2013.12.008.

Bresciani, M., Adamo, M., de Carolis, G., Matta, E., Pasquariello, G., Vaiciute, D., Giardino, C., 2014. Monitoring blooms and surface accumulation of cyanobacteria in the Curonian Lagoon by combining MERIS and ASAR data. Remote Sens. Environ. 146, 124–135. https://doi.org/10.1016/j.rse.2013.07.040.

Cho, C.H., 1991. Mariculture and eutrophication in Jinhae bay. Korea. Mar. Pollut. Bull. 23, 275–279. https://doi.org/10.1016/0025-326X(91)90687-N.

Diaz, R.J., Rosenberg, R., 2008. Spreading dead zones and consequences for marine ecosystems. Science 321, 926–929. https://doi.org/10.1126/science.1156401.

Doney, S.C., 2010. The growing human footprint on coastal and open ocean biogeochemistry. Science 321, 1512–1516. https://doi.org/10.1126/science.1185198.

Hong, G.H., Kim, K.T., Pae, S.J., Kim, S.H., Lee, S.H., 1991. Annual cycles of nutrients and dissolved oxygen in a nutrient-rich temperate coastal bay, Chinhae Bay. Korea. J. Korean Soc. Oceanogr. 26, 204–222.

Howarth, R., Chan, F., Conley, D.J., Garnier, J., Doney, S.C., Marino, R., Billen, G., 2011. Coupled biogeochemical cycles: eutrophication and hypoxia in temperate estuaries and coastal marine ecosystems. Front. Ecol. Environ. 9, 18–26. https://doi.org/10.1890/100008.

Hu, C., Lee, Z., Franz, B., 2012. Chlorophyll *a* algorithms for oligotrophic oceans: A novel approach based on three-band reflectance difference. J. Geophys. Res. 117 (C1) https://doi.org/10.1029/2011jc007395.

Hwang, J.H., Jang, D., Kim, Y.H., 2017. Stratification and salt-wedge in the Seomjin River Estuary under the idealized tidal influence. Ocean. Sci. J., https://doi.org/10.1007/s12601-017-0050-3.

Hwang, J.H., Van, S.P., Choi, B.J., Chang, Y.S., Kim, Y.H., 2014. The physical processes in the Yellow Sea. Ocean and Coastal Management 102, 449–457.

Jang, P., Lee, W., Jang, M., Lee, J., Lee, W., Jang, M., Hwang, K., Shin, K., 2005. Spatial and temporal distribution of inorganic nutrients and factors controlling their distributions in Gwangyang Bay. Ocean Polar Res. 27, 359–379.

Jang, P., Jang, M., Lee, W., Shin, K., 2010. Effects of nutrient property changes on summer phytoplankton community structure of Jangmok Bay. Ocean Polar Res. 32, 97–111. https://doi.org/10.4217/OPR.2010.32.2.097.

Jordan, T.E., Correll, D.L., Miklas, J., Weller, D.E., 1991. Nutrients and chlorophyll at the interface of a watershed and an estuary. Limnol. Oceanogr. 36, 251–267.

Kemp, W.M., Boynton, W.R., 1992. Benthic-pelagic interactions: nutrient and oxygen dynamics. In: Smith, D.E. (Ed.), Oxygen Dynamics in the Chesapeake Bay. Maryland Sea Grant College, Maryland, pp. 149–221.

Kilpatrick, K.A., Podesta, G., Walsh, S., Williams, E., Halliwell, V., Szczodrak, M., Brown, O.B., Minnett, P.J., Evans, R., 2015. A decade of sea surface temperature from MODIS. Remote Sens. Environ. 165, 27–41. https://doi.org/10.1016/j.rse.2015.04.23.

Kim, D.-S., 1999. Oceanic condition of fishing ground in the southwestern coastal sea of Korea in 1998. Bull. Korea Fish. Tech. Soc. 35 (3), 291–300.

Kim, D., Baek, S.H., Yoon, D.-Y., Kim, K.-H., Jeong, J.-H., Jang, P.-G., Kim, Y.-O., 2014a. Water quality assessment at Jinhae Bay and Gwangyang Bay. South Korea. Ocean Sci. J. 49, 251–264. https://doi.org/10.1007/s12601-014-0026-5.

Kim, J.B., Lee, S.Y., Yu, J., Choi, Y.H., Jung, C.-S., Lee, P.-Y., 2006. The characteristics of oxygen deficient water mass in Gamak Bay. J. Korean Soc. Mar. Environ. Energy 9, 216–224.

Kim, J.B., Hong, S., Lee, W.-C., Lee, Y.-W., Kim, H.C., Cho, Y., 2015a. Evaluation of phytoplankton community composition in the eutrophic Masan Bay by HPLC pigment analysis. J. Environ. Biol. 36, 491–498.

Kim, Y.H., Im, J., Ha, H.K., Choi, J.K., Ha, S., 2014b. Machine learning approaches to coastal water quality monitoring using GOCI satellite data. GISci. Remote Sen. 51, 158–174. https://doi.org/10.1080/15481603.2014.900983.

Kim, D., Lee, C.-W., Choi, S.-H., Kim, Y.O., 2012a. Long-term changes in water quality of Masan Bay. Korea. J. Coast. Res. 28, 923–929. https://doi.org/10.2112/JCOASTRES-D-11-00165.1.

Kim, S.-Y., Lee, Y.-H., Kim, Y.-S., Shim, J.-H., Ye, M.-J., Jeon, J.-W., Hwang, J.-R., Jun, S.-H., 2012b. Characteristics of marine environmental in the hypoxic season at Jinhae Bay in 2010. Korea J. Nat. Conserv. 6 (2), 115–129. https://doi.org/10.11624/KJNC.2012.6.2.115.

Kim, Y.-S., Lee, Y.-H., Kwon, J.-N., Choi, H.-G., 2015b. The effect of low oxygen conditions on biogeochemical cycling of nutrients in a shallow seasonally stratified bay in southeast Korea (Jinhae Bay). Mar. Pollut. Bull. 95, 333–341. https://doi.org/10.1016/j.marpolbul.2015.03.022.

Kim, D.S., Rho, H.K., 1993. Environmental factors and catch fluctuation of set-net grounds in the coastal water of Yeosu. 1. Oceanographic condition in the vicinity of set-net ground. Bull. Korea Fish. Tech. Soc. 29, 1–10.

Kim, D.S., Rho, H.K., 1994. Environmental factors and catch fluctuation of set-net grounds in the coastal water of Yeosu. 2. Sea water circulation in the vicinity of set-net ground. Bull. Korea Fish. Tech. Soc. 30, 142–149.

Kim, H.-C., Son, S., Kim, Y.-H., Khim, J., Nam, J., Chang, W.-K., Lee, J.-H., Lee, C.-H., Ryu, J., 2017. Remote sensing and water quality indicators in the Korean West coast: Spatio-temporal structures of MODIS-derived chlorophyll-a and total suspended solids. Mar. Pollut. Bull. 121, 425–434. https://doi.org/10.1016/j.marpolbul.2017.05.026.

Kim, Y.H., Son, S., Kim, H.-C., Kim, B., Park, Y.G., Nam, J.H., Ryu, J., 2020. Application of satellite remote sensing in monitoring dissolved oxygen variabilities: A case study for coastal waters in Korea. Env. Inter. 134, 105301 https://doi.org/10.1016/j.envint.2019.105301.

Kong, G.S., Park, S.C., 2007. Paleoenvironmental changes and depositional history of the Korea (Tsushima) Strait since the LGM. Journal of Asian Earth Sciences 29 (1), 84–104.

Kwon, S.J., Kang, T.S., 2007. Numerical simulation for behavior of tidal elevation and tidal currents in the south sea. J. Korean Soc. Coast. Ocean Eng. 19 (3), 253–265.

Kwon, J.-N., Lee, J., Kim, Y., Lim, J.-H., Choi, T.-J., Ye, M.-J., Jun, J.-W., Kim, S., 2014. Long-term variations of water quality in Jinhae Bay. J. Korean Soc. Mar. Environ. Energy 17, 324–332. https://doi.org/10.7846/JKOSMEE.2014.17.4.324.

Lau, N.C., 1988. Variability of the observed midlatitude storm tracks in relation to low-frequency changes in the circulation pattern. J. Atmos. Sci. 45, 2718–2743. https://doi.org/10.1175/1520-0469(1988)045<2718:VOTOMS>2.0.CO;2.

Lee, H.J., Jo, H.R., Chu, Y.S., Bahk, K.S., 2004. Sediment transport on macrotidal flats in Garolim Bay, west coast of Korea: significance of wind waves and asymmetry of tidal currents. Cont. Shelf Res. 24, 821–832.
Lee, J., Jung, R., Kim, S., Ko, W., Kim, K., Park, J., Lee, Y., 2001. Limiting Nutrient on Phytoplankton Growth in Gwangyang Bay. J. Korean Soc. Oceanogr. 6, 201–210.
Lee, M.-O., Kim, J.-K., 2008. Characteristics of algal blooms in the southern coastal waters of Korea. Mar. Environ. Res. 65, 128–147. https://doi.org/10.1016/j.marenvres.2007.09.006.
Lee, J., Kim, S.-G., An, S., 2017. Dynamics of the physical and biogeochemical processes during hypoxia in Jinhae Bay, South Korea. J. Coast. Res. 33, 854–863. https://doi.org/10.2112/JCOASTRES-D-16-00122.1.
Lee, A., Kim, S.Y., Min, H.S., 2019. Climatological descriptions on regional circulation around the Korean Peninsular. Tellus A: Dynamic Meteor. And Oceano. 71, 1. https://doi.org/10.1080/16000870.2019.1604058.
Lee, M.O., Lee, S.H., Kim, P.J., Kim, B.K., 2018a. Characteristics of water masses and its distributions in the southern coastal waters of Korea in summer. J. Korean Soc. Mar. Environ. Energy 21, 76–96. https://doi.org/10.7846/JKOSMEE.2018.21.2.76.
Lee, J., Park, K.-T., Lim, J.-H., Yoon, J.-E., Kim, I.-N., 2018b. Hypoxia in Korean coastal waters: A case study of the natural Jinhae Bay and artificial Shihwa Bay. Front. Mar. Sci. 5, 70. https://doi.org/10.3389/fmars.2018.00070.
Lim, H.-S., Diaz, R.J., Hong, J.-S., Schaffner, L.C., 2006. Hypoxia and benthic community recovery in Korean coastal waters. Mar. Pollut. Bull. 52, 1517–1526. https://doi: 10.1016/j.marpolbul.2006.05.013.
Linkin, M., Nigam, S., 2008. The North Pacific Oscillation–west Pacific teleconnection pattern: Mature-phase structure and winter impacts. J. Climate 21, 1979–1997. https://doi.org/10.1175/2007JCLI2048.1.
Lu, X., Hu, Y., Yang, Y., Bontempi, P., Omar, A., Baize, R., 2020. Antarctic spring ice-edge blooms observed from space by Icesat-2. Remote Sens. Environ. 245, 111827 https://doi.org/10.1016/j.rse.2020.111827.
Minnett, P.J., Evans, R.H., Podesta, G.P., Kilpatrick, K.A., 2014. Sea-surface temperature from Suomi-NPP VIIRS: Algorithm development and uncertainty estimation. Proc. SPIE 9111. https://doi.org/10.1117/12.2053184.
Mouw, C.B., Greb, S., Aurin, D., DeGiacomo, P.M., Lee, Z., Twardowski, M., Binding, C., Hu, C., Ma, R., Moore, T., Moses, W., Craig, S.E., 2015. Aquatic color radiometry remote sensing of coastal and inland waters: Challenges and recommendations for future satellite missions. Remote Sens. Environ. 160, 15–30. https://doi.org/10.1016/j.rse.2015.02.001.
Nakamura, H., Tanaka, M., Wallace, J.M., 1987. Horizontal structure and energetics of Northern Hemisphere wintertime teleconnection patterns. J. Atmos. Sci. 44, 3377–3391. https://doi.org/10.1175/1520-0469(1987)044,3377:HSAEON.2.0.CO;2.
Nigam, S., 2003. Teleconnections. In: Curry, J.A., Pyle, J.A. (Eds.), Encyclopedia of Atmospheric Sciences. Academic Press, pp. 2243–2269.
O'Reilly, J.E., et al., 2000. SeaWiFS Postlaunch calibration and validation analyses, Part 3. NASA Tech. Memo. 2000-206892, Vol. 11, S.B. Hooker and E.R. Firestone, Eds., NASA Goddard Space Flight Center p. 49.
Pak, G., Park, Y.-H., Vivier, F., Kwon, Y.-O., Chang, K.-I., 2014. Regime-dependent nonstationary relationship between the East Asian winter monsoon and North Pacific Oscillation. J. Climate 27, 8185–8204. https://doi.org/10.1175/JCLI-D-13-00500.1.
Park, M.O., Lee, Y.W., Ahn, J.B., Kim, S.S., Lee, S.M., 2017. Spatiotemporal distribution characteristics of temperature and salinity in the coastal area of Korea in 2015. J. Korean Soc. Mar. Environ. Energy. 20 (4), 226–239. https://doi.org/10.7846/JKOSMEE.2017.20.4.226.
Park, Y.-G., Seo, S., Kim, D.G., Noh, J., Park, H.M., 2021. Coastal observation using a vertical profiling system at the southern coast of Korea. Front. Mar. Sci. 8, 668733 https://doi.org/10.3389/fmars.2021.668733.
Park, Y.A., Yi, H.-I., 1995. Late Quaternary Climatic Changes and Sea-level History along the Korean Coasts. J. Coast. Res. Spec. Issue No. 17, 163–168.
Rabalais, N.N., Turner, R.E., Wiseman, W.J., 2002. Gulf of Mexico hypoxia, A.K.A. The Dead Zone. Ann. Rev. Ecol. Syst. 33, 235–263. https://doi.org/10.1146/annurev.ecolsys.33.010802.150513.
Rosenzweig, C., Casassa, G., Karoly, J.D., Imeson, A., Liu, C., Menzel, A., Rawlins, S., Root, L.T., Seguin, B., Tryjanowski, P., 2007. Assessment of observed changes and responses in natural and managed systems. Climate change: Impacts, adaptation and vulnerability. In contribution of working group II to the fourth assessment report of the Intergovernmental Panel on Climate Change 79–131.
Ryther, J.C., Dunstan, W.M., Tenore, K.R., Huguenin, J.E., 1972. Controlled eutrophication-increasing food protection from the sea by cycling human wastes. Bio-science 22, 144–152.
Seo, S., Park, Y.-G., 2020. Destination of floating plastic debris released from ten major rivers around the Korean Peninsula. Environemt International 138, 105655.
Siswanto, E., Tang, J., Yamaguchi, H., Ahn, Y.-H., Ishizaka, J., Yoo, S., Kim, S.-W., Kiyomoto, Y., Yamada, K., Chiang, C., Kawamura, H., 2011. Empirical ocean-color algorithms to retrieve chlorophyll-a, total suspended matter, and colored dissolved organic matter absorption coefficient in the Yellow and East China Seas. J. Oceanogr. 67, 627–650.
Son, S., Kim, Y.H., Kwon, J.-I., Kim, H.-C., Park, K.-S., 2014. Characterization of spatial and temporal variation of suspended sediments in the Yellow and East China Seas using satellite ocean color data. GISci. Remote Sen. 51, 212–226. https://doi.org/10.1080/15481603.2014.895580.
Stumpf, R., Arnone, R., Gould, R., Martinolich, P., Ransibrahmanakul, V., 2003. A partially coupled ocean–atmosphere model for retrieval of waterleaving radiance from SeaWiFS in coastal waters. SeaWiFS Postlaunch Technical Report Series. In S. B. Hooker, & E. R. Firestone (Eds.), NASA Tech. Memo. 2003–206892, 22. P. 51–59. Greenbelt, Maryland: NASA Goddard Space Flight Center.
Takaya, K., Nakamura, H., 2005a. Mechanisms of intraseasonal amplification of the cold Siberian high. J. Atmos. Sci. 62, 4423–4440. https://doi.org/10.1175/JAS3629.1.
Takaya, K., Nakamura, H., 2005b. Geographical dependence of upper-level blocking formation associated with intraseasonal amplification of the Siberian high. J. Atmos. Sci. 62, 4441–4449. https://doi.org/10.1175/JAS3628.1.
Takaya, K., Nakamura, H., 2013. Interannual variability of the East Asian winter monsoon and associated modulations of the planetary waves. J. Climate 26, 9445–9461. https://doi.org/10.1175/JCLI-D-12-00842.1.
Tanaka, S., Nishii, K., Nakamura, H., 2016. Vertical structure and energetics of the western Pacific teleconnection pattern. J. Climate 29, 6597–6616. https://doi.org/10.1175/JCLI-D-15-0549.1.
Teague, W.J., Jacobs, G.A., Perkins, H.T., Book, J.W., Chang, K.I., Suk, M.S., 2002. Low-frequency current observations in the Korea/Tsushima Strait. J. Phys Oceanography v. 32: 6, 1621–1641.
Wallace, J.M., Gutzler, D.S., 1981. Teleconnections in the geopotential height field during the Northern Hemisphere winter. Mon. Wea. Rev. 109, 784–812. https://doi.org/10.1175/1520-0493(1981)109<0784:TITGHF>2.0.CO;2.
Walton, C.C., Pichel, W.G., Sapper, J.F., May, D.A., 1998. The development and operational application of nonlinear algorithms for the measurement of sea surface temperatures with the NOAA polar-orbiting environmental satellites. J. Geophys. Res. 103 (C12), 27992–28012. https://doi.org/10.1029/98JC02370.
Wang, L., Chen, W., 2014. An intensity index for the East Asian winter monsoon. J. Climate 27, 2361–2374. https://doi.org/10.1175/JCLI-D-13-00086.1.
Yang, S.-K., 1994. Variation of the sea surface temperature distribution and the shelf fronts in the Cheju Strait and the Korea Strait. J. Korean Environ. Sci. Soc. 3, 35–42.
Yang, Y.J., Kim, S.H., Rho, H.K., 1998. A study on the temperature front observed in the south-west sea of Korea and the northern area of the East China sea. J. Korean Fish. Soc. 31, 695–706.
Yoo, D.G., Hong, S.H., Lee, G.S., Kim, J.C., Yoon, H.H., Cheong, D., 2020. Stratigraphic evolution of the Nakdong River valley in response to late Quaternary sea-level changes. Marine Geology 427, 106243.
Yoon, J.-E., Lim, J.-H., Son, S., Youn, S.-H., Oh, H.-J., Hwang, J.-D., Kwon, J.-I., Kim, S.-S., Kim, I.-N., 2019. Assessment of satellite-based chlorophyll-a algorithms in eutrophic Korean coastal waters: Jinhae Bay case study. Front. Mar. Sci. 6, 359. https://doi.org/10.3389/fmars.2019.00359.
Yuan, J., Tan, B., Feldstein, S.B., Lee, S., 2015. Wintertime North Pacific teleconnection patterns: Seasonal and interannual variability. J. Climate 28, 8247–8263. https://doi.org/10.1175/JCLI-D-14-00749.1.